Search for entrance channel effects in the decay of the ^{164}Yb compound nucleus at $E^* \approx 54$ MeV

J. L. Barreto,* N. G. Nicolis, D. G. Sarantites, R. J. Charity, L. G. Sobotka, and D. W. Stracener
Department of Chemistry, Washington University, St. Louis, Missouri 63130

D. C. Hensley, J. R. Beene, C. Baktash, M. Halbert, and M. Thoennessen†
Oak Ridge National Laboratory, Oak Ridge, Tennessee 37830
(Received 9 July 1993)

The existence of entrance channel effects in the decay of ^{164}Yb*, formed at $E^* \approx 54$ MeV in the reactions ^{16}O + ^{148}Sm and ^{64}Ni + ^{100}Mo is investigated. Evaporation residue cross sections, entry state γ-ray fold distributions as well as energy and angular distributions of exit-channel selected charged particles were obtained for each reaction, using 4π detection systems for both particles and γ rays. In the ^{64}Ni-induced reaction, the center-of-mass α-particle angular distributions were found to be symmetric around 90° indicating emission from a fully equilibrated compound nucleus. However, the corresponding angular distributions in the ^{16}O-induced reaction show a forward component which exclusively affects the population of the αxn residue channels. The γ-ray fold distributions for the αxn and xn channels show differences depending on the entrance channel as reported previously for similar systems. These differences can be understood in terms of contributions from the equilibrium decay of incompletely fused ^{16}O with ^{148}Sm and the mapping of the compound nucleus spin distributions, obtained from realistic fusion models, to the evaporation residue γ-ray fold distributions. It is concluded that the initial population of the compound nucleus is the only reason for the observed differences in the decay of ^{164}Yb* populated in these reactions.

PACS number(s): 25.70.Gh, 25.70.Jj, 24.60.Dr

I. INTRODUCTION

The Bohr hypothesis [1] concerning the independence of the formation and decay of a compound nucleus has proved to be a cornerstone in the understanding of fusion reactions. This concept presumes that the excitation process leaves the nucleus in a sufficiently complex state so that the subsequent decay is statistical and independent of the formation process. Implementation of this hypothesis in the statistical model has been successful in describing a large volume of experimental data concerning the decay of compound nuclei formed in heavy-ion fusion reactions [2].

Despite this success, some studies have questioned the Bohr hypothesis because of an apparent failure of the model to account for certain reaction characteristics. In particular, an unexpected dependence of the decay of the compound nucleus on the mode of formation was observed [3–6].

Neutron evaporation spectra and associated multiplicities were measured by Kühn *et al.* [3] for the reaction of 233 MeV ^{64}Ni + ^{92}Zr $\rightarrow$ ^{156}Er*. The statistical model was unable to describe simultaneously the slopes of the energy spectra and the cross sections for the xn channels. It was speculated that the compound nucleus is trapped in a superdeformed minimum during the shape relaxation process. Thus some of the excitation energy is tied up in deformation energy during the neutron emission time. When this effect was included in the statistical model, using elevated yrast lines resembling those of a superdeformed nucleus, it provided an improved description of the neutron cross sections. It was suggested that such a mechanism could be verified in a study of fusion reactions if entrance channels with different mass asymmetries were used to create the same compound nucleus. Fusion models predict that entrance channels of small mass asymmetries pass through more deformed configurations and are thus more likely to be trapped in the superdeformed minima. Janssens *et al.* [4] measured excitation functions of evaporation residue cross sections and neutron multiplicity distributions in the ^{12}C + ^{144}Sm and ^{64}Ni + ^{92}Zr reactions, leading to the same compound nucleus ^{156}Er. Statistical model calculations were able to account for the data in the ^{12}C-induced but not in the ^{64}Ni-induced reaction, in which the neutron multiplicities were systematically overpredicted. These results were in agreement with subsequent measurements of fission yields in the ^{64}Ni + ^{92}Zr reaction [6].

An alternative interpretation emerged from the realization that the dynamics of the fusion process significantly affects the angular momentum distributions of massive systems [7]. Average γ-ray multiplicities and cross sections for neutron evaporation channels were measured by Haas *et al.* [8] for reactions with various mass asymmetries leading to ^{160}Er compound nuclei at bombarding energies near the barrier. These data found an explanation in terms of barrier fluctuations which result in compound

*On leave from Instituto de Física da UFRJ - CP 21945-RJ, Brazil.
†Present Address: National Superconducting Cyclotron Laboratory and Department of Physics and Astronomy, Michigan State University, East Lansing, MI 48824.

nucleus angular momentum distributions wider than the predictions of a simple one-dimensional barrier penetration model. This leads to a reduction in the average effective temperature of the decaying system, an effect equivalent to using a narrower angular momentum distribution in conjunction with elevated yrast lines in the statistical model.

A similar interpretation was drawn from the work of Love *et al.* [9] who measured γ-ray multiplicity distributions of evaporation residues in the reaction 236 MeV ^{64}Ni + ^{92}Zr. The study of the feeding pattern ruled out the possibility of trapping in superdeformed states as a cause of the reported anomaly in the reproduction of the neutron cross sections [3]. A compound nucleus angular momentum distribution derived from simple coupled-channel calculations was introduced in the statistical model and found adequate to account for the observed neutron multiplicities.

In order to distinguish between the two interpretations, Ruckelshausen *et al.* [5] performed measurements of the evaporation residue angular momentum distributions in the decay of the ^{156}Er compound nucleus produced at the excitation energy of 47 MeV in the reactions ^{12}C + ^{144}Sm and ^{64}Ni + ^{92}Zr. Strong differences in the αxn and high spin xn populations were observed. For the xn channels in particular, the ratio of the $2n/3n$ cross sections as a function of the compound nucleus spin was found to depend on the entrance channel, suggesting that there is memory of the mode of formation in the particle evaporation process.

The presence of entrance channel effects in the early fusion dynamics [10] is relevant here, because reactions involving entrance channels with different mass asymmetry can lead to differences in the early stages of the decay process. Suitable probes, such as γ-ray emission in the giant resonance region, can be used to observe these differences as it was done in the work of Thoennessen *et al.* [11]. Whether these early dynamics effects can alter the xn cross-section ratios or the neutron multiplicities is questionable. Surprisingly, recent measurements of emitted charged particles and high-energy γ rays in the ^{12}C + ^{144}Sm and ^{64}Ni + ^{92}Zr reactions producing ^{156}Er* (47 MeV) failed to observe a dependence on entrance channel asymmetry [12].

Clearly, a satisfactory understanding of all these effects is still lacking. In order to shed some light on this subject, we performed a detailed study of the decay of the compound nucleus ^{164}Yb formed at the initial excitation energy of $E^* \approx 54$ MeV in the reactions ^{16}O + ^{148}Sm and ^{64}Ni + ^{100}Mo. In this study we made use of light charged particle detection in a 4π geometry [13]. Furthermore, evaporation residue γ-ray fold distributions and total γ-ray information were obtained with the spin spectrometer [14]. These measurements were made in coincidence with discrete γ transitions in the evaporation residues detected by an array of Ge detectors. The shapes of the spectra and angular distributions of the emitted charged particles combined with the γ-ray fold distributions of evaporation residues provide a complete set of data for the comparison of the two reactions.

The particle and γ-ray information obtained in this work is used to address the following issues: (a) establish the origin of the displacement in spin of the populations of the αxn channels in the asymmetric and nearly symmetric reaction, (b) understand the high spin behavior of the evaporation residue entry state populations of the xn channels, and (c) examine the possibility of observing anomalously large anisotropies in low-energy α-particle emission as an evidence for emission from an elongated compound nucleus configuration [16]. If found, such distinctions between the two reactions could give a more definite answer to the question of the existence of entrance channel effects put forward in Refs. [3–5].

Preliminary results of this work have been reported previously [17]. The present work extends a previous study [18] where the decay of ^{164}Yb* formed in the reaction ^{64}Ni + ^{100}Mo was studied at lower bombarding energies. In Sec. II we describe details of the experimental methods. The experimental results and their comparison with model calculations are given in Secs. III and IV. The conclusions are summarized in Sec. V.

II. EXPERIMENTAL PROCEDURES

Heavy-ion beams of ^{64}Ni ($E_{\rm lab}$ = 242.0 MeV) and ^{16}O ($E_{\rm lab}$ = 87.0 MeV) bombarded targets of ^{100}Mo and ^{148}Sm, respectively. The beams were provided by the Holifield Heavy-Ion Research Facility. Typical beam intensities measured at the Faraday cup were $\sim$ 45 enA for ^{64}Ni- and $\sim$ 7.7 enA for ^{16}O. The targets were self-supporting metallic foils of Mo (306 μg/cm^2, enriched to 97.27% in ^{100}Mo) and Sm (968 μg/cm^2, enriched to 96.40% in ^{148}Sm). The beam energy loss through these targets was estimated to be $\approx$ 5.89 MeV (in ^{100}Mo) and $\approx$ 2.02 MeV (in ^{148}Sm), taking into account the 63.4° angle between the target surface and the beam. The effective beam energies were estimated to be 239.1 MeV and 86.0 MeV in the ^{64}Ni- and ^{16}O-induced reactions, respectively. They correspond approximately to the beam energies in the middle of the targets. These estimates are based on the bombarding energy dependence of theoretical fusion cross sections which are consistent with the total evaporation residue cross sections extracted in the present experiment. The initial excitation energies of the compound nucleus ^{164}Yb* were calculated to be 53.4 MeV and 54.4 MeV in the ^{64}Ni- and ^{16}O-induced reactions, respectively. In the following discussion we will refer to the compound nucleus ^{164}Yb* as being formed at the initial excitation energy of 54 MeV.

Light charged particles (p, d, ^{3}He, α) emitted in these reactions were detected by the Dwarf Ball. The Dwarf Ball, a nearly 4π CsI(Tl) scintillator array [13], consists of 70 equal solid angle detectors covering laboratory angles from $\theta_{\rm lab}$ = 12° to 168°. The detectors are arranged in 14 rings of 5 detectors each at $\phi_{\rm lab}$ angles separated by 72°. Detectors which belong in the same ring correspond to the same $\theta_{\rm lab}$. A total of 14 different laboratory angular ranges are sampled. Besides angular distributions, the energy spectra of the emitted protons and α particles were also obtained. Energy calibrations for protons were made using elastic and inelastic scattering measurements

of 14.0 MeV protons on a 80 μg/cm^2 self-supporting ^{12}C target. For α particles, the energy calibration at high energies was obtained from the proton energy calibration using the empirical relationships of Ref. [13]. This calibration was matched at low energies to three calibration points (6.287, 6.777, and 8.785 MeV) measured with a ^{232}U source. The solid angle of the Dwarf Ball detectors was measured with a ^{249}Cf source. For this purpose, the fraction of the 5.812 MeV α particles detected in coincidence with the 333.3 and 388.1 keV γ rays by each detector was measured. The average solid angle per detector was found to be 0.92 of $4\pi/72$.

In order to stop elastically scattered projectiles inside the grazing angle ($\theta_{\rm lab} \approx 75°$) and reduce the number of δ electrons from the target, Ta absorbers were placed in front of the CsI(Tl) detectors. The absorber thicknesses ranged from 26.0 mg/cm^2 for the forward to 2.5 mg/cm^2 for the backward detectors. The resulting thresholds for forward emitted α particles and protons were 8 and 2 MeV for the ^{64}Ni-induced reactions and 10 MeV and 3 MeV for the ^{16}O-induced reactions, respectively. At backward angles, the thresholds were 2 and 1 MeV for α particles and protons, for both reaction systems.

Residual nuclei were identified by their discrete transitions, detected with 18 Compton-suppressed Ge detectors that replaced 18 elements of the spin spectrometer [14]. Table I shows the characteristic γ-ray transitions used to identify these residues. In the present experiments, a Ge pulse was always required to make an event trigger. Scaled-down events, where the Ge detector was the only trigger, were stored in order to provide data for the (HI,xn) channels. The scaled-down factor was adjusted in order to equalize approximately the rates of γ-particle coincidences and γ-ray singles stored during the data aquisition. The Ge detectors were calibrated for energy and efficiency using standard γ-ray sources of ^{152}Eu, ^{60}Co, ^{88}Y, ^{133}Ba, and ^{182}Ta.

The γ-ray multiplicity distributions for each identified exit channel were measured using 52 NaI(Tl) detectors of the spin spectrometer. In addition, the 18 Compton-suppression shields of the Ge detectors were used as a part of the γ-multiplicity array. For the NaI(Tl) detectors of the spin spectrometer good identification of neutron and γ-ray pulses was achieved by time of flight, using the average "t_0" procedure described in Ref. [14].

TABLE I. Gamma transitions for evaporation residues observed in this work.

Residue	Channel	E_γ (keV)	Transition	Δk[a]
^{162}Yb	$2n$	320.6	$4^+ \rightarrow 2^+$	1.00
^{161}Yb	$3n$	232.2	$\frac{17}{2}^+ \rightarrow \frac{13}{2}^+$	2.75
^{160}Yb	$4n$	244.0	$2^+ \rightarrow 0^+$	
^{159}Yb	$5n$	300.0	$\frac{17}{2}^+ \rightarrow \frac{13}{2}^+$	3.00
^{161}Tm	$p2n$	162.7[b]	$\frac{13}{2}^- \rightarrow \frac{11}{2}^-$	
^{160}Tm	$p3n$	176.5[b]	$12^- \rightarrow 11^-$	
^{158}Er	$\alpha 2n$	192.1	$2^+ \rightarrow 0^+$	
^{157}Er	$\alpha 3n$	266.4	$\frac{17}{2}^+ \rightarrow \frac{13}{2}^+$	2.75

[a]Shift applied in the corresponding fold distributions.
[b]Most intense transition.

For the anti-Compton shields, the limited timing resolution prevented the complete identification of neutron and γ-ray pulses. Energy and efficiency calibrations of the spin spectrometer detectors were obtained using γ-ray sources of ^{207}Bi, ^{88}Y, ^{60}Co, ^{208}Tl (in equilibrium with ^{232}U) according to the procedures of Ref. [14]. The response functions of the spin spectrometer providing the γ-ray multiplicity (M_γ) as a function of the γ-ray coincidence fold (k_γ) were obtained using data from the above sources in the equal energy approximation [14].

Absolute cross sections were measured by integrating the beam current and correcting for the average effective charges $\bar{q}_{\rm Ni} = 21.3$ and $\bar{q}_{\rm O} = 7.24$, determined for equilibrated projectile charge states in their passage through the target [15]. The systematic error in the cross sections reported below is estimated to be $\simeq 19\%$. This error includes an estimated 12% error in the average projectile charge, 8% for the target thickness, 8% for the solid angle per detector, 7% for the Ge detector efficiencies, and 6% for the charge integration.

The present experimental setup offered the ability to study the energy and angular distributions of the emitted charged particles in coincidence with specific evaporation residues selected by their discrete γ transitions. The spin spectrometer made possible the study of the above quantities as a function of the associated γ-ray fold, or γ-ray multiplicity, which is related to the entry state spin and then to the compound nucleus spin.

III. EXPERIMENTAL RESULTS

A. Charged particle energy spectra and angular distributions

The measured angular and energy distributions of emitted protons and α particles were transformed event-by-event in the center-of-mass (c.m.) system assuming two-body kinematics. Energy spectra of the emitted α particles were obtained in the c.m. energy range from 13 to 30 MeV. Figure 1 shows the α-particle c.m. spectra for selected angles, measured in coincidence with the $2^+ \rightarrow 0^+$ transition in ^{158}Er for both reactions. The spectra shown correspond to a forward, a near 90°, and a backward c.m. angle and were selected with the requirement that the γ-ray fold, $k_\gamma \geq 5$. They were obtained by summing the spectra from detectors at the same polar angle. The angles indicated in Fig. 1 result from an averaging due to the finite opening of the detectors and the energy dependence in the transformation to the c.m. system. In both reactions, the energy spectra show a peak around 18 MeV. At similar $\theta_{\rm c.m.}$ angles, the α2n yield is found to be higher in the ^{16}O- than in the ^{64}Ni-induced reaction. We also note that in the ^{64}Ni + ^{100}Mo reaction the shapes of the forward and backward spectra are similar. However, in the ^{16}O + ^{148}Sm reaction the forward spectra are considerably more energetic than the backward ones.

Total angular distributions in the c.m. system were obtained by integrating the energy spectra at each angle. The resulting angular distributions for the αxn and

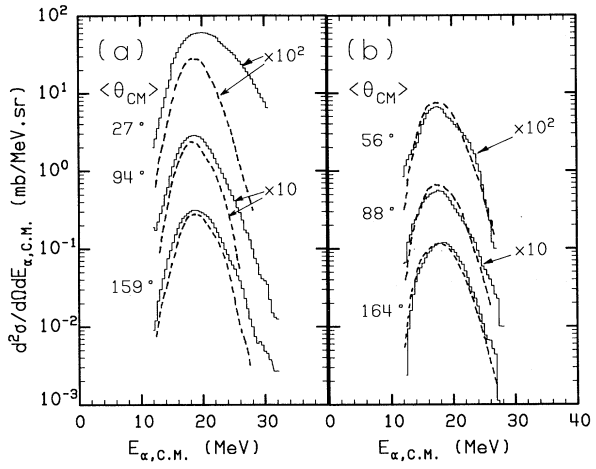

FIG. 1. The histograms on (a) and (b) show the double-differential cross sections $d^2\sigma/d\Omega dE_{\alpha,\mathrm{c.m.}}$ versus $E_{\alpha,\mathrm{c.m.}}$ of α particles from the $\alpha 2n$ exit channel at the indicated center-of-mass angles, for the ^{16}O + ^{148}Sm and the ^{64}Ni + ^{100}Mo reactions, respectively. The calculated energy spectra from the equilibrium decay of ^{164}Yb* are shown by the dashed lines for both reactions.

$p3n$ channels are shown by the symbols in Fig. 2. In the ^{64}Ni + ^{100}Mo system [see Fig. 2(b)], the $\alpha 2n$ and $\alpha 3n$ are the only charged particle channels with measurable yields in coincidence with the discrete γ-ray transitions. For ^{16}O + ^{148}Sm [Fig. 2(a)], besides these two channels, the ^{160}Tm ($p3n$) channel could also be identified with a measurable cross section. In the ^{64}Ni + ^{100}Mo system, the $\alpha 2n$ and $\alpha 3n$ angular distributions are symmetric around $\theta_{\mathrm{c.m.}} = 90°$. This pattern is characteristic of emission from a fully equilibrated compound nucleus. However, in the ^{16}O + ^{148}Sm system, both of these channels show rather different patterns with an extra forward component. This forward peaked component is stronger in the $\alpha 2n$ than the $\alpha 3n$ channel. Yet the proton angular distribution, for the $p3n$ channel, is symmetric around $\theta_{\mathrm{c.m.}} = 90°$ consistent with emission from an equilibrated compound nucleus.

These observations indicate the existence of a nonstatistical mechanism which contributes to the $\alpha 2n$ and $\alpha 3n$ populations in the ^{16}O + ^{148}Sm reaction. There is also a strong dependence of the angular distributions on the α-particle energy. This is demonstrated in Fig. 3 for the $\alpha 2n$ channel. The c.m. angular distributions are plotted for different bins in the α-particle energy. The lines represent fits of the data to an expansion in terms of Legendre polynomials of the form

$$W(\theta_{\mathrm{c.m.}}) = A_0[1 + A_1 P_1(\theta_{\mathrm{c.m.}}) + A_2 P_2(\theta_{\mathrm{c.m.}})], \quad (1)$$

where A_0, A_1, and A_2 are free parameters. As can be seen in Fig. 3, the forward contribution is present for all particle energies and increases strongly with increasing α-particle energy. Therefore, we conclude that the forward component in the angular distributions of the αxn channels in the ^{16}O-induced reaction is dominated by the most energetic α particles.

The emission of these high-energy α particles is strongly enhanced in the lower γ-ray folds of the αxn channels. The thick histogram in Fig. 4 shows the total α-particle spectrum observed at $\theta_{\mathrm{c.m.}} = 27°$. It includes contributions from $k_\gamma \geq 5$. The various thin line histograms show the decomposition of this spectrum into contributions from the indicated k_γ bins. The α-particle

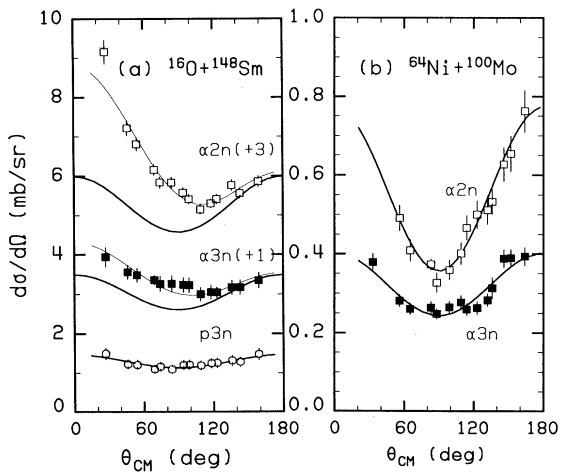

FIG. 2. Experimental (symbols) center-of-mass angular distributions of channel-gated α particles and protons in the ^{64}Ni + ^{100}Mo and ^{16}O + ^{148}Sm reactions. The thick lines show the fit of Eq. (1) to the data. The thin lines correspond to the estimated equilibrium component, see text. The angular distributions of the αxn channels in the ^{16}O + ^{148}Sm reaction have been shifted upward by the offsets given in parentheses.

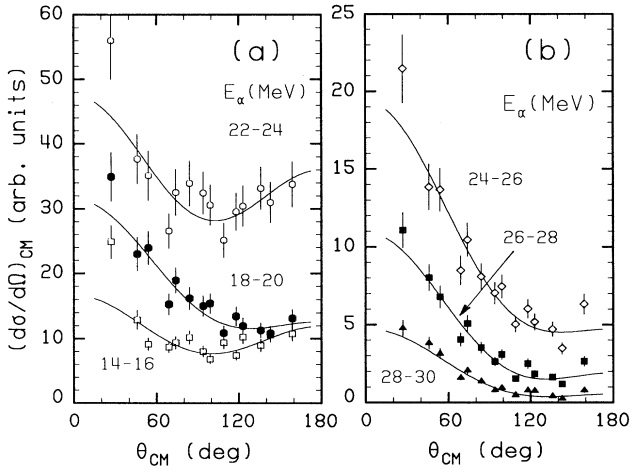

FIG. 3. Center-of-mass angular distributions of α particles associated with the $\alpha 2n$ channel in the ^{16}O + ^{148}Sm reaction. In (a) the open squares, solid circles, and open circles correspond to the α-energy bins of 14–16, 18–20, and 22–24 MeV, respectively. In (b) the open diamonds, solid squares, and solid triangles correspond to α-energy bins of 24–26, 26–28, and 28–30 MeV, respectively. The curves in both panels represent fits of Eq. (1) to the data.

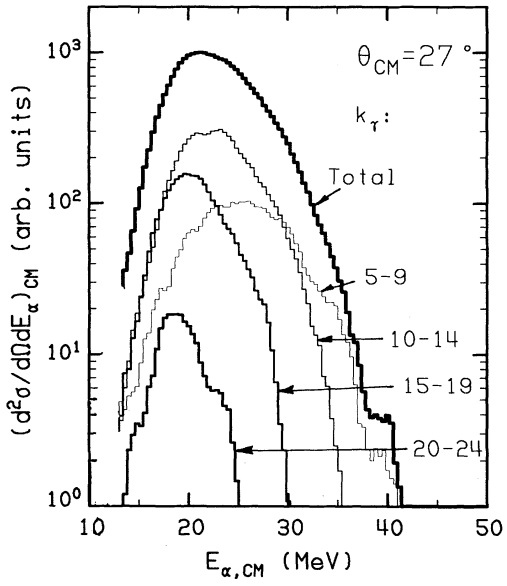

FIG. 4. Total α-particle spectrum (thickest histogram) from the $\alpha 2n$ channel (for $k_\gamma \geq 5$) observed at the most forward angle in the reaction $^{16}O + ^{148}Sm$. The thinner lined histograms give the decomposition of the total spectrum in terms of k_γ according to the indicated k_γ gates.

spectrum corresponding to the lowest k_γ bin has a strong high-energy contribution. This contribution is progressively reduced as k_γ increases.

The nonequilibrium component may be associated with an incomplete fusion process in which the ^{16}O projectile breaks up into $^{12}C + \alpha$, followed by fusion of the ^{12}C with the target nucleus. The subsequent decay of the resulting $^{160}Er^*$ by emission of two or three neutrons contributes to the $\alpha 2n$ and $\alpha 3n$ channels under study. This nonequilibrium component also affects the entry state distributions of these channels. Specifically, it shifts the k_γ distributions to values lower than those associated with the equilibrium decay of $^{164}Yb^*$ (see Secs. III C and IV A).

The above finding provides a rational explanation to the previously reported differences in the evaporation residue spin distributions involving αxn emission [5]. In the previous studies [3,5], the strongest shifts in the spin distributions with entrance channel mass asymmetry were observed in ^{12}C bombardments; i.e., a projectile that could also lead to incomplete fusion with an α ejectile. The possibility of incomplete fusion in these measurements was mentioned in Ref. [5].

The total angular distributions for the αxn channels from the $^{64}Ni + ^{100}Mo$ reaction were fitted with the Legendre polynomial expansion of Eq. (1), with the A_1 term set equal to zero. The extracted parameters A_0 and A_2 are given in Table II. The resulting fits are shown as solid curves in Fig. 2(b). Cross sections obtained by integrating Eq. (1) were found in agreement with those extracted from discrete γ-ray measurements (Sec. III B).

Decomposition of the forward peaked angular distributions for the $^{16}O + ^{148}Sm$ reaction, although not a simple matter, could provide the equilibrium cross sections for α-particle emission from $^{164}Yb^*$. Such a decomposition was made based on the assumption that equilibrium emission represents the observed angular distributions at $\theta_{c.m.} = 180°$. Since lower spins are involved in the $^{16}O + ^{148}Sm$ reaction, the A_2 coefficients for equilibrium α-particle emission were assumed to be 85% of the values extracted from the $^{64}Ni + ^{100}Mo$ reaction. Then, using Eq. (1) (with A_1=0), a value for the A_0 coefficient was obtained (Table II). The results of this decomposition are shown by the thick solid curves in Fig. 2(a) for the αxn channels in the $^{16}O + ^{148}Sm$ reaction. The extracted cross sections of the statistical components are given in Table III. Due to our assumption that there is no contribution from the breakup component at $\theta_{c.m.} = 180°$, these values represent the maximum contributions from compound nucleus emission.

The formation of long-lived superdeformed configurations at high spin, in the more symmetric entrance channel, has been suggested [3,4,6] as a possible explanation for the effects observed in those experiments. We examined the possibility of using the anisotropy of the emitted low-energy α particles as a probe of an elongated configuration in the emitting system. For a nearly spherical decaying nucleus, the anisotropy of the emitted α particles is predicted to decrease with decreasing particle energy. In contrast, the anisotropy is expected to increase if the emitting nucleus is deformed [16]. Earlier measurements and interpretations of such effects were based on anisotropies with respect to the estimated spin direction. A similar effect is expected to be observed in the distributions with respect to the beam direction (see Ref. [16] and references therein). If there are deformation effects persisting during the α-emission times involved, then we should be able to observe an increasing anisotropy in the angular distributions for low-energy α emission. This test was performed using the $\alpha 2n$ channel in the $^{64}Ni + ^{100}Mo$ reaction. The center-of-mass α-particle angular distributions for this channel are shown in Fig. 5, for

TABLE II. Legendre polynomial coefficients of α-particle and proton angular distributions in coincidence with the αxn and $p3n$ channels in the $^{16}O + ^{148}Sm$ and $^{64}Ni + ^{100}Mo$ reactions.

Reaction	$^{16}O + ^{148}Sm$			$^{64}Ni + ^{100}Mo$	
Channel	$\alpha 2n$[a]	$\alpha 3n$[a]	$p3n$[b]	$\alpha 2n$	$\alpha 3n$
A_0	1.93 ± 0.19	1.79 ± 0.13	1.18 ± 0.02	0.55 ± 0.02	0.28 ± 0.02
A_2	0.46 ± 0.04	0.31 ± 0.03	0.18 ± 0.03	0.54 ± 0.05	0.36 ± 0.04

[a]Values corresponding to the extracted statistical component (Sec. III A).
[b]Corresponding to the most intense transition (Table I).

TABLE III. Experimental cross sections for the observed decay channels in the ^{64}Ni + ^{100}Mo and ^{16}O + ^{148}Sm reactions. For the latter system, the extracted equilibrium components of the αxn cross sections are also indicated. The reported errors are statistical. The estimated systematic errors of 19% are not included.

Decay channel	^{64}Ni + ^{100}Mo (mb)	^{16}O + ^{148}Sm (mb)
$2n$	24 ± 4	1.5 ± 0.6
$3n$	86 ± 7	177 ± 10
$4n$	93 ± 9	529 ± 32
$5n$		14 ± 3
$p2n$	6.5 ± 1.4	19 ± 4
$p3n$	9.4 ± 1.5	48 ± 8
$\alpha 2n$	7.6 ± 1.6	32 ± 4
		25 ± 5[a]
$\alpha 3n$	3.4 ± 1.2	26 ± 4
		23 ± 4[a]
σ_{ER}	230 ± 11	835 ± 31[b]

[a]Extracted equilibrium component (Section III A).
[b]Total evaporation residue cross section including only the extracted equilibrium component.

three different energy bins. These angular distributions were fitted to Eq. (1) with A_1=0 and the anisotropy coefficients A_2 were extracted. A plot of the A_2 coefficients versus the average α-particle energy is shown in Fig. 6(a). The experimental anisotropy generally decreases with decreasing α-particle energy in agreement with a pattern characteristic of emission from a nearly spherical system. However, an analysis of α-particle spectra with the statistical model (see Sec. IV B and Fig. 6(b)] indicates that the lowest α-particle energies in the $\alpha 2n$ channel are associated with the latest stages of the deexcitation. This implies that the observed low-energy anisotropies do not provide a sensitive probe of nuclear deformation during the first emission steps.

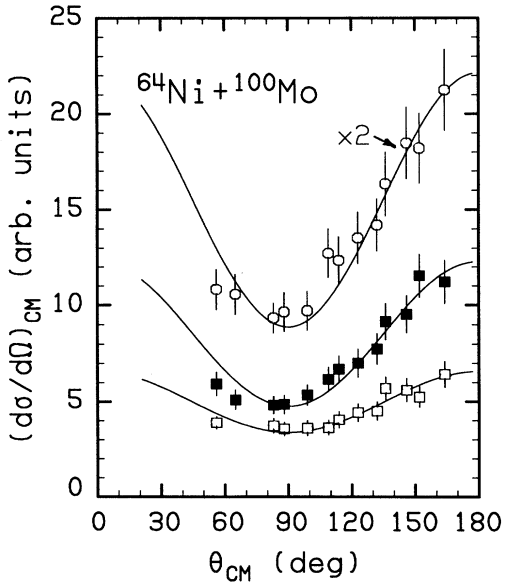

FIG. 5. Center-of-mass angular distributions for the $\alpha 2n$ exit channel in the ^{64}Ni + ^{100}Mo reaction as a function of α-particle energy. The open squares, solid squares, and open circles correspond to E_α in the ranges 14–16, 16–18, and 18–20 MeV, respectively. Fits with a symmetric Legendre polynomial expansion are shown by the solid lines.

B. The evaporation residue cross sections

Table III lists the measured evaporation residue cross sections for the xn, pxn and αxn channels in the ^{64}Ni + ^{100}Mo and ^{16}O + ^{148}Sm reactions. In the former system, the cross sections for most of the channels were obtained from the discrete γ-ray transitions given in Table I. The $p2n$ and $p3n$ cross sections represent sums of yields from several rotational bands [19,20]. For the $p3n$ channel, the most prominent γ peak is from the $12^- \rightarrow 11^-$ (176.7 keV) transition. The level scheme [20] indicates that the population of the known negative-parity levels flows only partially through the 12^- state, with a $13^- \rightarrow 11^-$ (329.5 keV) transition by-passing this state. A similar situation appears in the known positive-parity levels [20]. The cross section for the $p3n$ channel was obtained by summing the yields of the 329.5 keV, and 176.7 keV for the negative-parity yrast band, and 381.2 keV, 312.8 keV, 210.6 keV, and 170.7 keV for the positive-parity band. A 10% correction for a few low-level missing transitions in the ^{160}Tm residue was applied.

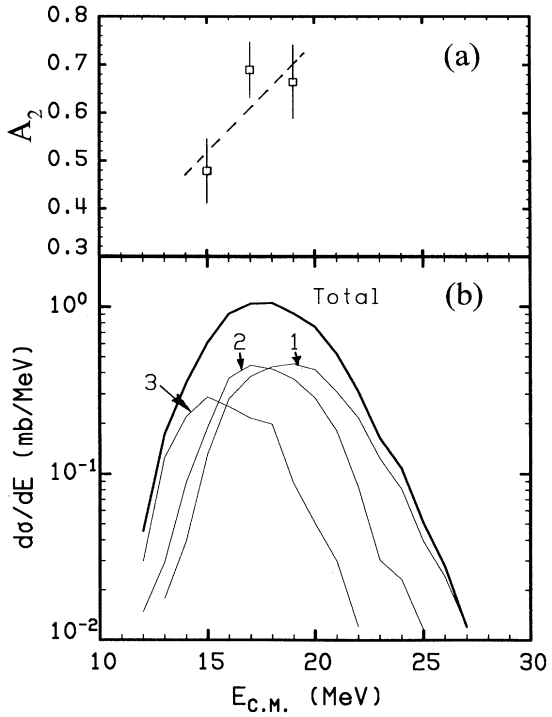

FIG. 6. (a) shows the experimental A_2 coefficients as a function of the average α-particle energy, extracted from the fits shown in Fig. 5. The dashed line is drawn to guide the eye. (b) gives the calculated center-of-mass α-particle spectrum corresponding to the $\alpha 2n$ channel (thick line) and its decomposition to contributions from emissions at different α emission steps (indicated by the numbers shown).

The extraction of the ^{161}Tm($p2n$) cross section is also complex. We observe lines at 322.6 keV ($\frac{15}{2}^- \rightarrow \frac{11}{2}^-$), 159.9 keV ($\frac{15}{2}^- \rightarrow \frac{13}{2}^-$), and 162.7 keV ($\frac{13}{2}^- \rightarrow \frac{11}{2}^-$) for the two signature partners [20] of the negative-parity 7/2[523] band. Measurable yields for the transitions from the 1/2[411], 1/2[541], and 7/2[404] side bands could not be obtained. The total cross section was obtained by summing the yields of the 322.6 keV, 159.9 keV, and 162.7 keV transitions and applying an arbitrary correction of 20% to take into account any missing transitions in this channel. Due to the low yield in this decay channel, it was not possible to obtain the γ-ray fold distributions in either reaction.

In the ^{16}O + ^{148}Sm reaction the total αxn cross sections, obtained by gating on the discrete γ-ray transitions of the residues, contain contributions from the breakup component of the projectile. Table III gives the total αxn cross sections and the estimated equilibrium contributions as described in the previous section.

C. The evaporation residue γ-ray fold distributions

Entry state distributions (in k_γ and total γ-ray pulse height, H_γ) of evaporation residues were extracted using the information provided by the spin spectrometer. The experimental k_γ distributions of certain evaporation residues were shifted upward by Δk in cases where the gating γ transition leads to a state of nonzero spin. This correction accounts for the number of γ rays that would have been emitted if the ground state of the residual nucleus (^{159}Yb) was zero, and for those low-energy transitions which are below the energy threshold of the spin spectrometer (^{161}Yb, ^{157}Er). It was assumed that $\Delta I = 2\Delta M_\gamma \approx 2\Delta k_\gamma$. This way, a direct comparison can be made between the experimental fold distributions and the calculated ones with the statistical model in which details of nuclear structure are ignored. The applied shifts are given in Table I.

Figures 7(a) and 7(d) show the experimental γ-ray fold distributions of various xn channels as a function of $k_{\rm eff} = k_\gamma + \Delta k$, for the two reactions. Apart from the difference in the absolute magnitude of the respective cross sections, we observe the following features. The k_γ distributions of the $4n$ channels have the same shape and peak position in both reactions. However, the $3n$ and $2n$ distributions are found to be at lower $k_{\rm eff}$ values in the ^{16}O + ^{148}Sm reaction. There is a difference of 2 to 3 units in the peak position of the $3n$ channel. A more pronounced difference of $\approx$ 5 units is observed in the $2n$ channel. These differences are similar to those reported in Ref. [5].

In order to compare the two reactions on the same ground we construct the cross-section ratios

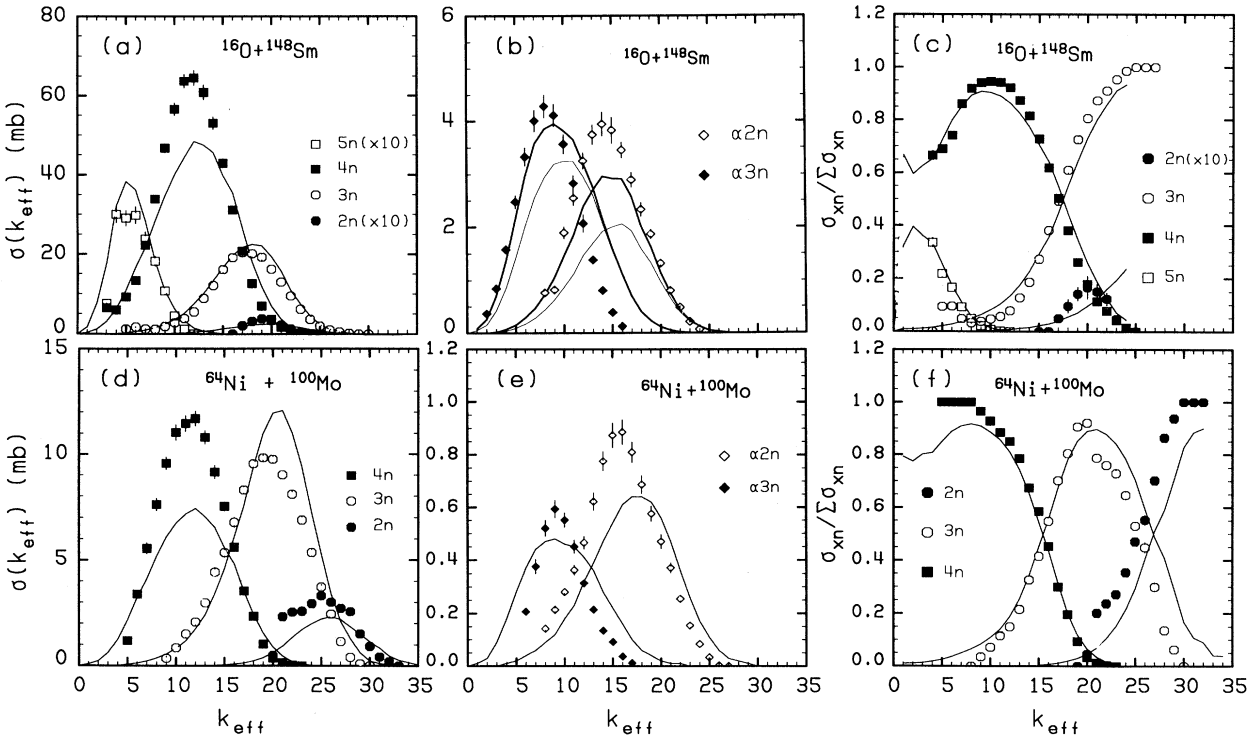

FIG. 7. The symbols on the top row (a)–(c) show the experimental cross sections for the xn, αxn channels, and cross-section ratios, $\sigma_i(k)/\Sigma\sigma_i(k)$, as a function of $k_{\rm eff}$, for the 86 MeV ^{16}O + ^{148}Sm reaction. The summation is over the xn channels that accounts for the bulk of the total cross section. The same quantities for the 239 MeV ^{64}Ni + ^{100}Mo reaction are shown in the lower half (d)–(f). The solid lines represent the results of the statistical model calculations described in the text.

$\sigma_i(k)/\Sigma\sigma_i(k)$, where the summation is taken over the xn channels which represent the bulk of the measured yields. These ratios are shown as a function of k_{eff} as data points in Figs. 7(c) and 7(f), and are compared in Fig. 8. The open and closed symbols correspond to the ^{16}O- and ^{64}Ni-induced reactions, respectively. Differences are now seen at all values of k_{eff}. For $k_{\text{eff}} < 8$, these are due to the absence of $5n$ cross section in ^{64}Ni + ^{100}Mo. The most dramatic differences occur at the highest γ folds, where the $2n$ channel is the strongest in the ^{64}Ni + ^{100}Mo reaction [see Figs. 7(c) and 7(f)], thus depleting completely the $3n$ contribution. In ^{16}O + ^{148}Sm, the weakness of the $2n$ channel causes the $3n$ ratio to dominate at high k_{eff}.

The k_{eff} distributions of the channels involving $\alpha 2n$ and $\alpha 3n$ emission are shown in Figs. 7(b) and 7(e), for both reactions. The k_{eff} distribution for the $\alpha 2n$ channel shows the largest downward shift, which can be explained quantitatively as due to the ^{16}O breakup as discussed in Secs. III A and IV A. Similarly, the $\alpha 3n$ channel shows a smaller downward shift for the ^{16}O reaction, which is consistent with the observed smaller contribution of the ^{16}O breakup-fusion process to this channel (Sec. III A). An attempt to describe quantitatively the k_{eff} distributions in terms of the two reaction mechanisms is presented in Sec. IV.

At first glance, the above differences could be interpreted as evidence for an entrance channel effect in the decay of the compound nucleus ^{164}Yb*. However, the independence of formation and decay of the compound nucleus has to be investigated in terms of the spin of the compound nucleus. One may make such a comparison given the fact that the evaporation residue k_{eff} distributions are available. In a first approach, one may attempt to deduce the compound nucleus spin distributions from the residue k_{eff} distributions. This procedure was followed in Refs. [5,18] using techniques similar to those developed in Refs. [21–23]. These techniques are best suited for the transformation of distribution *averages* and *not distributions*. Retrieving the compound nucleus angular momentum distribution involves transformations from k_γ to M_γ, then to the entry state spin, and finally to the compound nucleus spin.

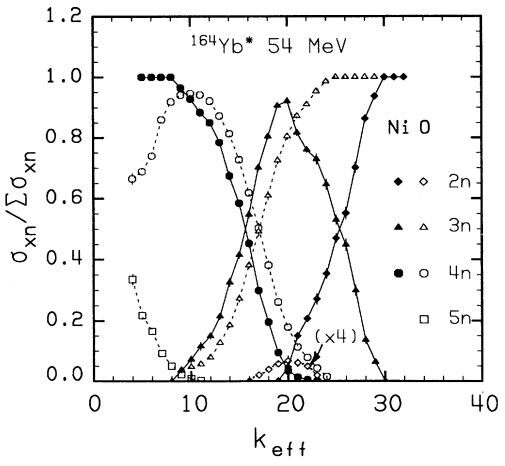

FIG. 8. Cross-section ratios $\sigma_i(k)/\Sigma\sigma_i(k)$ as a function of k_{eff}, for the $2n$, $3n$, $4n$, and $5n$ channels. The solid symbols refer to the ^{64}Ni + ^{100}Mo and the open symbols to the ^{16}O + ^{148}Sm reaction. The solid lines are for the ^{64}Ni-induced reactions and the dashed lines for the ^{16}O reactions. They are shown to guide the eye.

To avoid problems with consecutive unfoldings, which are not always unique, we have opted for the following approach. Through the use of appropriate reaction models we produce compound nucleus spin distributions (σ_ℓ) that lead to a reasonable agreement with the evaporation residue cross sections in statistical model calculations for both reactions. In these calculations, the entry state (E^*, I), and the (E^*, M_γ) distributions of each residue are obtained. By folding the (E^*, M_γ) distributions with the measured $(E^*, M_\gamma) \rightarrow (H_\gamma, k_\gamma)$ responses of the spin spectrometer, we obtain by projection the theoretical k_γ distributions which can be compared with the experimental ones.

IV. STATISTICAL MODEL CALCULATIONS

Statistical model calculations were performed for both systems of the present study in order to examine the extent to which the observed quantities are described in terms of the equilibrated decay of ^{164}Yb*. The statistical model parameters used were the same for both reactions. The compound nucleus angular momentum distributions were obtained from appropriate fusion models.

The calculations were performed with the code EVAP [24]. The level density formalism of Gilbert and Cameron [25] was employed with a level density parameter of $a = A/9.0$ MeV^{-1}. The choice of this value was made on the basis of agreement between calculated and experimental α-particle spectra measured for both reactions. It is consistent with the value used in a similar reaction in Ref. [26]. Penetrabilities for particle emission were calculated from the optical model using the global parametrizations of Wilmore and Hodgson [27], Perey [28], and McFadden and Satchler [29] for neutrons, protons, and α particles, respectively. In the description of γ competition, emission of $E1$, statistical and collective $E2$, $M1$, and $M2$ γ rays were included. The $E1$ γ-ray emission strength function included the giant dipole resonance (GDR) with shape and position taken from systematics [30,31] and strength determined by the classical energy weighted sum rule [30]. The GDR splitting due to deformation was included using a double Lorentzian GDR shape corresponding to an input prolate deformation parameter $\beta_{\text{GDR}} = 0.2$. The γ strengths for $M1$, statistical $E2$, $E2_{\text{coll}}$, and $M2$ were set equal to 0.01, 10.0, 100.0, and 1.2 W.u., respectively. Similar parameters to the above provide a good description of evaporation residue excitation functions in both reactions through the statistical model [32,33].

A. The ^{16}O + ^{148}Sm reaction

The measured fusion cross section at $E_{\text{lab}} = 86$ MeV was compared to and found to be consistent with the

lower-energy data of DiGregorio *et al.* [32]. The compound nucleus angular momentum distribution (σ_ℓ) at 86 MeV was produced by equating the experimental fusion cross section $\sigma_{\rm fus}$ with $\sum \sigma_\ell$, where

$$\sigma_\ell = \pi\lambda^2(2\ell+1)\left\{1+\exp\frac{\ell-\ell_0}{\Delta}\right\}^{-1}. \quad (2)$$

Here, λ is the asymptotic reduced wavelength and ℓ_0 was adjusted iteratively to obtain consistency between the calculated sum and the experimental evaporation residue cross sections. Using this procedure, a value of $\ell_0 = 38.2\hbar$ was extracted. The diffuseness parameter Δ was set equal to 1.5. This choice produces a good agreement between the measured cross sections of the xn channels with those calculated by the statistical model. Including the effect of target deformation in a fusion calculation would result in a more diffuse σ_ℓ distribution. However, the presence of incomplete fusion in the present experiment introduces some uncertainty in our knowledge of the upper edge of the σ_ℓ distribution. The energy loss of the beam through the target was taken into account by distributing the initial compound nucleus excitation energies uniformly over a range consistent with the beam energy loss.

The calculated evaporation residue cross sections are shown by the histograms in Fig. 9. They are compared to the data given by the symbols on the same figure. The overall agreement with the data is good. Some discrepancies appear as an underprediction of the $4n$ and an overprediction of the $5n$ and $2n$ yields. However, it has to be noted that our bombarding energy is close to the threshold for the $5n$ channel and to the energy where the $2n$ cross section falls off rapidly. This could explain the difficulty in the simultaneous reproduction of these two cross sections by the statistical model. The data points of the αxn cross sections in Fig. 9 correspond to the total measured cross sections and therefore include nonequilibrium contributions. We note that the $\alpha 2n$ cross section from the ^{16}O-induced reaction is underestimated by the equilibrium calculation.

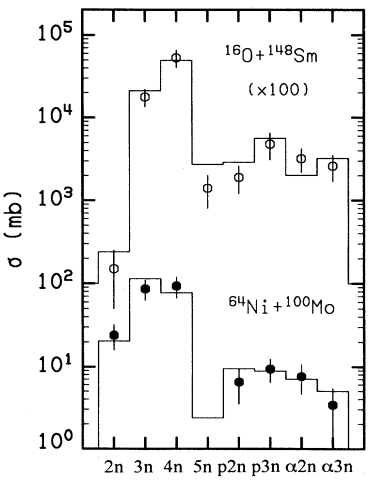

FIG. 9. Comparison between the total measured (symbols) and calculated (histograms) evaporation residue cross sections of the reactions under study. The errors bars include statistical and systematic errors.

For each of the evaporation residues, the calculated entry state distributions as a function of the excitation energy $E*$, and M_γ, were folded with the spin spectrometer response functions (obtained according to the procedures of Ref. [14]) to yield the corresponding distributions in H_γ and k_γ. The distributions in (H_γ, k_γ) were then projected on the k_γ axis to be compared with the experimental ones.

The comparison is shown in Fig. 7, where the solid lines represent the calculated distributions. The agreement with exit channels involving neutron evaporation [Fig. 7(a)] is good except for an underprediction of the 4n cross section. The total $\alpha 2n$ and $\alpha 3n$ k_γ distributions are also underestimated by this equilibrium calculation shown by the thin lines on Fig. 7(b). Underestimation of the total αxn distributions was expected in this case on the basis of the observed nonequilibrium α emission. Another difference occurs in the $\alpha 3n$ distribution which is predicted to extend to higher than the observed $k_{\rm eff}$ values.

Nonequilibrium α-particle emission should take place predominantly from very high ℓ waves. A calculation was made with the sum-rule model of Wilczyński [34] to estimate the excitation energy and angular momentum distribution of the resulting ^{160}Er* compound nucleus. These distributions were used as an input for an evaporation calculation for ^{160}Er*. The calculated $2n$ and $3n$ cross sections and angular momentum distributions were then added to those of the previous equilibrium calculation and compared to the total $\alpha 2n$ and $\alpha 3n$ data. The sum of the calculated distributions is shown by the thick lines on Fig. 7(b). The addition of the nonequilibrium component makes a substantial improvement in the description of the data.

From the calculated γ-ray fold distributions for the xn channels, the corresponding k_γ-gated cross-section ratios were extracted. They are shown by solid lines in Fig. 7(c) and compared to the data. A good agreement between theory and experiment is observed. The trend of the data as well as the crossing points of the ratios for different channels are reasonably well reproduced.

The equilibrium component of the calculated α-particle spectra (dashed lines) leading to the $\alpha 2n$ channel is compared with the center-of-mass experimental spectra in Fig. 1(a). The backward spectrum is fairly well reproduced in shape and magnitude by the calculation. The 94° spectrum is slightly underpredicted at all energies, indicating a small excess of α particles over those predicted to originate from an equilibrated compound nucleus. The comparison with the 27° spectrum shows clearly a large excess of α emission at all energies with respect to the calculated one. The existence of a high-energy nonequilibrium component is clearly evident.

Summarizing, we note that the overall features of the xn and pxn decay channels in the ^{16}O + ^{148}Sm reaction are reproduced with statistical model calculations employing reasonable parameters. For αxn channels, the

addition of the nonstatistical component brings a better agreement with the experimental data.

B. The ^{64}Ni + ^{100}Mo reaction

For the purpose of the calculations, the bombarding energy must be corrected for the energy loss through the target. The average energy was calculated using the energy dependence of the excitation function data of Ref. [18] augmented by the present total fusion cross section to provide a smooth empirical excitation function curve. In the statistical model calculations, the reaction was assumed to take place in five consecutive slices of the target, each $\approx$ 1.2 MeV thick. In each slice, the empirical cross section was used in a consistent way, according to the reduction of the beam energy in the previous slices. A beam energy spread of $\sim$ 1.0 MeV was also introduced within each slice. This procedure accounts for the effect of target thickness in the magnitude of the partial wave cross sections as well as the energy dependence of the maximum angular momentum for fusion. The results of the evaporation calculations were then averaged over the five slices.

Studies of the angular momentum distributions for fusion for this reaction at lower energies [18] have indicated that fusion occurs with much larger angular momenta than those predicted by the one-dimensional barrier penetration model. These extended angular momentum distributions are needed in order to reproduce the experimental cross sections for the $2n$, $3n$, and $4n$ channel cross sections. A simple way to demonstrate this effect is to vary the diffuseness of the compound nucleus angular momentum distribution on the calculated evaporation residue cross sections. Calculations were performed with diffuseness parameters Δ = 2.0, 3.0, 4.0, 6.0, 8.0, 10.0, and 12.0$\hbar$ in Eq. (2). Table IV gives the ratios of the experimental to the calculated evaporation residue cross sections, in each case. Due to the increasing fission competition with angular momentum, an adjustment in ℓ_0 was made in the last case (with Δ = 12.0$\hbar$, see Table IV) in order to bring agreement between the calculated and experimental sum of evaporation residue cross sections. As shown in Table IV the ratios for the $2n$, $3n$, and pxn channels tend towards unity with increasing diffuseness, indicating a better agreement with the experiment. This is related to the enhanced yield of high-ℓ partial waves allowed for fusion. We realize that a large diffuseness ($\Delta \sim 12.0\hbar$) leads to a suppression of low-ℓ partial waves. This results in an underprediction of the evaporation residue cross sections originating from low compound nucleus spins. This is consistent with the increase in the ratio for the $4n$ channel cross section with increasing Δ shown on Table IV. The αxn cross sections seem to be rather insensitive to variations in Δ.

The existence of high-ℓ components in the compound nucleus angular momentum distribution at energies near and below the fusion barrier is related to the enhancement of the experimental fusion cross section compared to the predictions of the one-dimensional barrier penetration model [7,35]. Mechanisms responsible for this enhancement include effects such as the static deformation of the reactants or coupling to inelastic or transfer channels. Coupled-channel calculations have been able to explain the enhancement of the subbarrier fusion cross sections and angular momentum distributions in many reaction systems. Inclusion of channel coupling causes a broadening of the angular momentum distributions even at energies above the barrier [7,35].

Calculations of the σ_ℓ distributions were performed with the channel-coupling code CCFUS [36]. For the extraction of the model parameters, the lower-energy fusion data [18] for the ^{64}Ni + ^{100}Mo reaction were taken into account. The code CCFUS includes the effect of coupling of the projectile and target inelastic and transfer degrees of freedom to the relative motion. A matrix diagonalization method including finite range effects is used for the solution of the multidimensional barrier penetration problem. Our calculations included the inelastic excitation of the low-lying 2^+ and 3^- states in the projectile and target using literature values [37,38] for the corresponding deformation parameters. Additional transfer coupling strengths [39] of F=3.5 and 2.5 MeV with Q values of -1 and -5 MeV, respectively, were introduced to describe the low-energy behavior of the fusion excitation function data of Ref. [18].

A statistical model calculation of the evaporation residue cross sections using the σ_ℓ distribution from CCFUS gave results similar to those obtained earlier with large diffuseness parameters ($\Delta \geq 6\hbar$). The ratios of the experimental to the calculated cross sections are given in the last column of Table IV. The use of the angular momentum distribution obtained with CCFUS leads to

TABLE IV. Ratios of the experimental to the calculated evaporation residue cross sections for different values of the diffuseness parameter Δ and the associated ℓ_0 values as introduced in Eq. (2).

Δ ($\hbar$)	2.0	3.0	4.0	6.0	8.0	10.0	12.0	CCFUS
ℓ_0 ($\hbar$)	47.6	47.6	47.2	46.5	45.5	44.3	45.3	
Channel								
$2n$	4.75	3.64	2.80	1.90	1.56	1.44	1.15	1.25
$3n$	0.76	0.76	0.77	0.80	0.85	0.89	0.83	0.81
$4n$	1.03	1.03	1.05	1.10	1.14	1.18	1.22	1.31
$p2n$	0.60	0.65	0.70	0.71	0.73	0.86	0.79	0.73
$p3n$	1.05	1.05	1.03	1.04	1.10	1.10	1.15	1.15
$\alpha 2n$	1.16	1.14	1.08	1.24	1.21	1.31	1.20	1.16
$\alpha 3n$	0.67	0.69	0.68	0.72	0.71	0.77	0.76	0.74

an improved description of the evaporation residue cross sections. In particular, the $2n$ cross section originating from very high spin is reasonably reproduced. However, this calculation underestimates the cross section of the low spin $4n$ channel. The comparison with the absolute magnitude of the evaporation residue cross-section data is shown in Fig. 9. In the following, we compare the rest of the experimental data with the results of this calculation.

The calculated γ-ray fold distributions are compared with the experimental ones in Fig. 7. The shape and peak position of the xn channels [Fig. 7(d)] are approximately reproduced. The discrepancies between the experimental and calculated distributions are primarily due to over- or under-predictions of the cross sections. The calculated distribution for the $\alpha 2n$ channel [Fig. 7(e)] peaks at a slightly higher value of k_γ and is more skewed than the experimental distribution. For the $\alpha 3n$ channel the peak position of the distribution is reproduced but the width is overestimated [Fig. 7(e)].

The experimental k_γ-fold cross-section ratios of the xn channels [Fig. 7(f)], are closely reproduced in the medium fold region $12 \leq k_{\text{eff}} \leq 20$. The deviations observed at higher folds are related to the overestimation and underestimation of the $3n$ and $2n$ yields, respectively.

The calculated α-particle spectra at the center-of-mass angles 56°, 88°, and 164° (leading to the $\alpha 2n$ channel) are compared with the experimental data in Fig. 1(b). They agree well in shape and peak position.

Next, we consider the contributions to the total calculated $\alpha 2n$ spectrum from α-particle emissions in different decay sequences. In Fig. 6(b), the spectrum shown with the thick line gives the total calculated center-of-mass spectrum associated with the $\alpha 2n$ channel. Its decomposition into contributions where the α particle is emitted first (αnn), second ($n\alpha n$), and third ($nn\alpha$) are given by the thin lines numbered according to the order of emission. The low-energy first chance α emissions do not contribute significantly to the low-energy part of the total $\alpha 2n$ spectrum. The presence of a deformation effect in the first stages of the deexcitation could be hidden in the background of lower energy α emissions occurring in the subsequent emission steps. Therefore, the observed α-particle anisotropies of the αxn channel do not provide a sensitive probe of nuclear deformations during the early stages of the deexcitation.

From the above discussion, we may conclude that the main features of the ^{64}Ni + ^{100}Mo reaction are reproduced by the statistical model using parameters that also describe the ^{16}O + ^{148}Sm reaction, the only difference being in the σ_ℓ distributions in each case. Inadequacies in describing details of the ^{64}Ni + ^{100}Mo data with the statistical model seem to relate with difficulties in modeling the compound nucleus angular momentum distribution in this reaction [18,33].

C. Comparison of the entrance and exit channel characteristics

Despite the fact that the compound nucleus ^{164}Yb* was produced at approximately the same initial excitation energy in both reactions, substantial differences occur in the populated angular momentum states. Part of these differences arises because of the entrance channel mass asymmetry. The nearly symmetric reaction ^{64}Ni + ^{100}Mo is more efficient in populating high angular momentum states in the compound nucleus. A further enhancement of the high-ℓ components occurs due to the coupling of inelastic and transfer degrees of freedom with the relative motion of ^{64}Ni and ^{100}Mo. The angular momentum distributions of the two reactions are best compared when plotted in terms of their reduced $(\sigma_\ell/\pi\lambda^2)$ values. This comparison is made in Fig. 10 which shows the reduced distributions employed in the present calculations. The angular momentum distribution for the ^{16}O + ^{148}Sm is consistent with a diffuseness parameter of Δ=1.5$\hbar$. It is compared with the result of an one-dimensional barrier penetration calculation for ^{64}Ni + ^{100}Mo (dashed curve labeled "uncoupled"). The corresponding fusion cross section is equal in magnitude to the sum of the experimental evaporation residue cross sections. Including the effect of channel coupling, as described in the previous section, produces the distribution labeled "coupled" in Fig. 10. The already high angular momentum content of the uncoupled distribution for ^{64}Ni + ^{100}Mo is amplified with the inclusion of channel coupling. Furthermore, there is a suppression of the low-ℓ partial waves in the region where this distribution overlaps with the one for the ^{16}O-induced reaction.

According to the independence hypothesis the decay from a specific compound nucleus state with spin I_{CN} from the same excitation energy should be independent of the entrance channel. In this work, however, distributions of cross sections as a function of k_γ were measured. These are related to the initial compound nucleus spins via several intermediate mappings that involve broad distributions. The effect of these broad distributions can easily lead to differences in the observed quantities with-

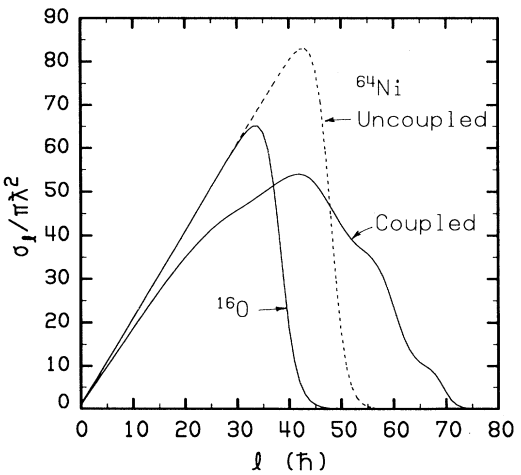

FIG. 10. Reduced spin distributions for the two reactions calculated using the one-dimensional barrier penetration model (curves labeled ^{16}O and ^{64}Ni uncoupled). For the ^{64}Ni + ^{100}Mo reaction, the effect of coupling to inelastic and transfer degrees of freedom is shown by the curve labeled coupled.

out violating the independence hypothesis. To demonstrate this, we compared the evolution of the initial populations in the decay of ^{164}Yb* as calculated with the statistical model for the two reactions. Figures 11(a)–(c) show the calculated ratios of the xn channel cross-section as a function of the entry state spin (I_{ER}), M_γ, and k_γ, respectively. Solid and dashed lines refer to the ^{64}Ni- and ^{16}O-induced reactions, respectively. The exit channels are indicated by the number of emitted neutrons. Note that these calculations have been able to describe

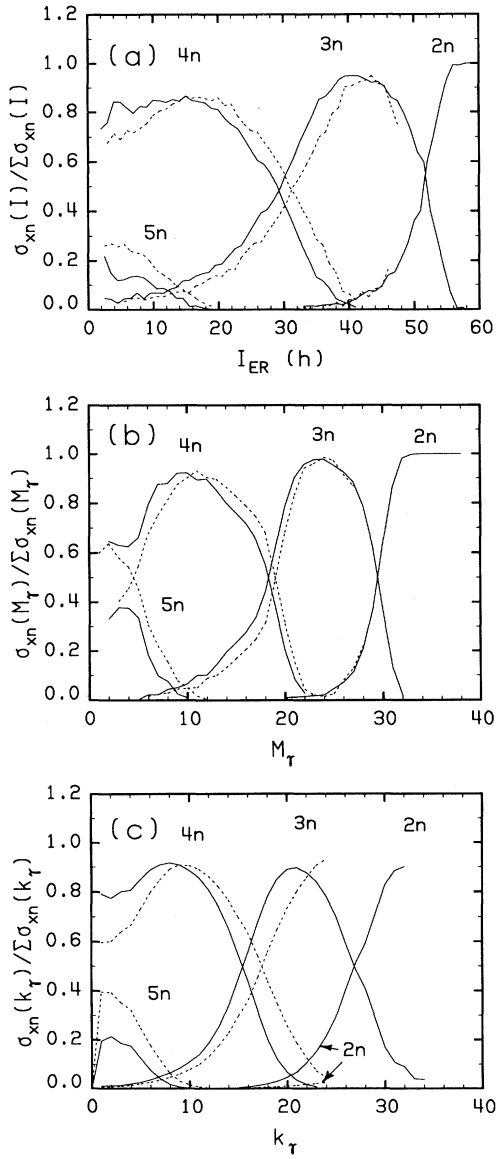

FIG. 11. Calculated cross-section ratios of the $2n$, $3n$, $4n$, and $5n$ channels as a function of (a) the evaporation residue spin I_{ER}, (b) the γ-ray multiplicity, M_γ, and (c) the γ-ray fold, k_γ, for the two reactions. Dashed lines refer to ^{16}O + ^{148}Sm and solid lines to ^{64}Ni + ^{100}Mo. Notice in particular the difference in the k_γ ratio between the two reactions for the $2n$ channel for $k_\gamma \geq 18$. Such a difference is absent in panel (b).

the experimental cross-section ratios as a function of k_γ, in both reactions. The calculated ratios as a function of I_{ER} for the ^{16}O-induced reaction are shifted up by almost 2 units in spin with respect to the ^{64}Ni-induced reaction [see Fig. 11(a)]. This *shift*, however, *is not due to violation* of the independence hypothesis. It is simply due to the fact that each entry state receives contributions from many intermediate states in excitation energy and angular momentum. The corresponding decay chains are weighted by the primary spin populations. A partial entry state cross section, $\sigma(I_{ER})$, results from a summation of all contributing cascades. The calculated cross-section ratios for the two reactions are influenced by the relative weights in the initial populations, which in turn are determined by the corresponding reduced angular momentum distributions.

The cross-section ratios after γ decay are shown in Fig. 11(b) as a function of M_γ. The difference between the solid and dashed curves has been reduced by almost a factor of 2, due to the quadrupole nature of the majority of the emitted γ radiation, as simulated in the evaporation code. Figure 11(c) gives the ratios as a function of k_γ. Compared with Fig. 11(b), it shows the effect of the spin spectrometer responses in the transformation of $M_\gamma \rightarrow k_\gamma$. As in the previous step ($I_{ER} \rightarrow M_\gamma$), the relations in the ratios of the major channels is retained. The only large difference is seen in the σ_{2n} / $\Sigma\sigma_{xn}$ ratio. Although the σ_{2n} / $\Sigma\sigma_{xn}$ ratios are identical as a function of M_γ in both reactions, they show sharp differences as a function of k_γ. This difference is attributed to the small magnitude of the $2n$ cross section in the ^{16}O-induced reaction and the fact that it corresponds to the highest M_γ values. In this case, the tails of the spin spectrometer responses (for the $M_\gamma \rightarrow k_\gamma$ conversion) introduce a spread in the shape of the extracted k_γ distribution. Clearly, the differences observed for the various exit channels in the two reactions are not related to any violation of the independence hypothesis.

As a general comment, the decay characteristics of both reactions expressed as σ_{xn} / $\Sigma\sigma_{xn}$ ratios are retained in the transformation from entry state spin to multiplicity and then to γ-ray fold. It was verified that the trends shown are not affected by the omission of pxn or the αxn channels in the construction of the cross-section ratios. Differences in the ratios as a function of the entry state spin for the two reactions are predicted by the statistical model calculation that takes into account the independence hypothesis.

V. SUMMARY

In the present work, we made use of a 4π detection of light charged particles and γ rays in an investigation of heavy-ion reaction mechanisms. This method provided a powerful means of comparing the deexcitation mechanism of ^{164}Yb* formed with $\approx$ 54 MeV of initial excitation in the nearly symmetric ^{64}Ni + ^{100}Mo and asymmetric ^{16}O + ^{148}Sm fusion reactions.

Differences in the entry states populated by xn and αxn emission were observed in the two reactions. The

effect in the αxn populations was attributed to an incomplete fusion mechanism present in the $^{16}O + ^{148}Sm$ reaction. The breakup component of the projectile was found to account for a large fraction of the total observed cross section in the $\alpha 2n$ channel, and for only a small fraction in the $\alpha 3n$ channel.

On the basis of the observed α-particle anisotropies for the $\alpha 2n$ channel, no definite conclusion can be drawn on a possible deformation effect in the first stages of the compound nucleus decay in the $^{64}Ni + ^{100}Mo$ reaction.

Differences in the γ-ray fold distributions of the xn channels populated in the two reactions were also observed. This result was consistent with the population of a broad compound nucleus spin distribution in the ^{64}Ni-induced reaction, as predicted by current fusion models. In the statistical model description of the compound nucleus decay, it was assumed that this is the only difference in the formation of $^{164}Yb^*$ in the two reactions. Based on this assumption, all of the experimental features were essentially understood without the need to resort to strong structural influences on the deexcitation of the compound nucleus by particle emission.

ACKNOWLEDGMENTS

J.L.B. wishes to acknowledge travel support from CNPq - Brazil. This work was supported by the Director, Office of Energy Research, Office of High Energy and Nuclear Physics, Nuclear Physics Division of the US Department of Energy, under Contract Nos. DE-FG02-88-ER40406 and DE-FG02-87-ER40316. Oak Ridge National Laboratory is managed by Martin Marietta Energy System, Inc. under Contract No. DE-AC05-84OR21400 with the Department of Energy.

[1] N. Bohr, Nature (London) **137**, 344 (1936).

[2] R. G. Stokstad, *Treatise on Heavy-Ion Science* (Plenum Press, New York, 1985), Vol. 3, p. 83.

[3] W. Kühn, P. Chowdhury, R. V. F. Janssens, T. L. Khoo, F. Haas, J. Kasagi, and R. M. Ronningen, Phys. Rev. Lett. **51**, 1858 (1983).

[4] R. V. F. Janssens, R. Holzmann, W. Henning, T. L. Khoo, K. T. Lesko, G. S. F. Stephans, D. C. Radford, A. M. Van den Berg, W. Kühn, and R. M. Ronningen, Phys. Lett. B **181**, 16 (1986).

[5] A. Ruckelshausen, R. D. Fischer, W. Kühn, V. Metag, R. Mühlhans, R. Novotny, T. L. Khoo, R. V. F. Janssens, H. Gröger, D. Habs, H. W. Heyng, R. Repnow, D. Schwalm, G. Duchène, R. M. Freeman, B. Haas, F. Haas, S. Hlavac, and R. S. Simon, Phys. Rev. Lett. **56**, 2356 (1986); A. Ruckelshausen *et al.*, **58**, 1584 (1987).

[6] F. L. H. Wolfs, R. V. F. Janssens, R. Holzmann, T. L. Khoo, W. C. Ma, and S. J. Sanders, Phys. Rev. C **39**, 865 (1989).

[7] R. Vandenbosch, Annu. Rev. Nucl. Part. Sci. **42**, 447 (1992).

[8] B. Haas, G. Duchène, F. A. Beck, T. Byrski, C. Gehringer, J. C. Merdinger, A. Nourredine, V. Rauch, J. P. Vivien, J. Barrette, S. Tobbeche, E. Bozek, J. Styczen, J. Keinonen, J. Dudek, and W. Nazarewicz, Phys. Rev. Lett. **54**, 398 (1985).

[9] D. J. Love, P. J. Bishop, A. Kirwan, P. J. Nolan, D. J. Thornley, A. H. Nelson, and P. J. Twin, Phys. Rev. Lett. **57**, 551 (1986); D. J. Love *et al.*, *ibid.* **58**, 1585 (1986).

[10] H. Feldmeier, Rep. Prog. Phys. **50**, 915 (1987).

[11] M. Thoennessen, J. R. Beene, F. E. Bertrand, C. Baktash, M. L. Halbert, D. J. Horen, D. G. Sarantites, W. Spang, and D. W. Stracener, Phys. Rev. Lett. **70**, 4055 (1993); M. Thoennessen, J. R. Beene, R. L. Auble, F. E. Bertrand, C. Baktash, M. L. Halbert, D. J. Horen, C. A. Ludemann, D. G. Sarantites, D. W. Stracener, and W. Spang, in Proceedings of the Workshop on Nuclear Structure and Heavy-Ion Reaction Dynamics [Instrum. Phys. Conf. Ser. No. **109**, 135 (1990)] Chap. 5; M. Thoennessen and J. R. Beene, in *Advances in Nuclear Dynamics*, Proceedings of the 8th Winter Workshop on Nuclear Dynamics, Jackson Hole, Wyoming, edited by W. Bauer and B. Back (World Scientific, Singapore, 1992), p. 1.

[12] B. Fornal, F. Gramegna, G. Prete, G. D'Erasmo, E. M. Fiore, A. Pantaleo, V. Paticchio, G. Viesti, P. Blasi, F. Lucarelli, M. Anghinolfi, P. Corvisiero, M. Taiuti, A. Zucchiatti, P. F. Bortignon, Ch. Ferrer, G. Nardelli, and G. Nebbia, Phys. Rev. C **42**, 1472 (1990).

[13] D. W. Stracener, D. G. Sarantites, L. G. Sobotka, J. Elson, J. T. Hood, Z. Majka, V. Abenante, A. Chbihi, and D. C. Hensley, Nucl. Instrum. Methods A **294**, 485 (1990).

[14] M. Jääskeläinen, D. G. Sarantites, R. Woodward, F. A. Dilmanian, J. T. Hood, R. Jääskeläinen, D. C. Hensley, M. L. Halbert, and J. H. Barker, Nucl. Instrum. Methods **204**, 385 (1983).

[15] K. Shima, T. Ishihara, and T. Mikumo, Nucl. Instrum. Methods **200**, 605 (1982).

[16] N. G. Nicolis, D. G. Sarantites, L. A. Adler, F. A. Dilmanian, K. Honkanen, Z. Majka, L. G. Sobotka, Z. Li, T. M. Semkow, J. R. Beene, M. L. Halbert, D. C. Hensley, J. B. Natowitz, R. P. Schmitt, D. Fabris, G. Nebbia, and G. Mouchaty, Phys. Rev. C **41**, 2118 (1990).

[17] J. L. Barreto, D. G. Sarantites, R. J. Charity, N. G. Nicolis, L. G. Sobotka, D. W. Stracener, D. C. Hensley, J. R. Beene, M. L. Halbert, and C. Baktash, in *Advances in Nuclear Dynamics*, Proceedings of the 8th Winter Workshop on Nuclear Dynamics, Jackson Hole, Wyoming, edited by W. Bauer and B. Back (World Scientific, Singapore, 1992), p. 8.

[18] M. L. Halbert, J. R. Beene, D. C. Hensley, K. Honkanen, T. M. Semkow, V. Abenante, D. G. Sarantites, and Z. Li, Phys. Rev. C **40**, 2558 (1989).

[19] S. André, D. Barnéoud, C. Foin, J. Genevey, J. A. Pinston, B. Haas, J. P. Vivien, and A. J. Kreiner, Z. Phys. A **333**, 247 (1989).

[20] C. Foin, S. André, J. Genevey, S. Drissi, V. Ionescu, J. Kern, and M. Rast, Nucl. Phys. A **417**, 511 (1984).

[21] D. G. Sarantites, L. Westerberg, M. L. Halbert, R. A. Dayras, D. C. Hensley, and J. H. Barker, Phys. Rev. C **18**, 774 (1978).

[22] L. Westerberg, D. G. Sarantites, D. C. Hensley, R. A. Dayras, M. L. Halbert, and J. H. Barker, Phys. Rev. C **18**, 796 (1978).

[23] R. A. Dayras, R. G. Stokstad, C. B. Fulmer, D. C. Hensley, M. L. Halbert, R. L. Robinson, A. H. Snell, D. G. Sarantites, L. Westerberg, and J. H. Barker, Phys. Rev. Lett. **42**, 697 (1979).
[24] Code EVAP, by N. G. Nicolis, D. G. Sarantites, and J. R. Beene (unpublished), evolved from the code PACE by A. Gavron, Phys. Rev. C **21**, 230 (1980).
[25] A. Gilbert and A. G. W. Cameron, Can. J. Phys. **43**, 1446 (1965).
[26] D. G. Sarantites, M. Jääskeläinen, R. Woodward, F. A. Dilmanian, D. C. Hensley, J. H. Barker, J. R. Beene, M. L. Halbert, and W. T. Milner, Phys. Lett. **115B**, 441 (1982).
[27] D. Wilmore and P. E. Hodgson, Nucl. Phys. **55**, 673 (1964).
[28] F. G. Perey, Phys. Rev. **131**, 745 (1963).
[29] L. McFadden and G. R. Satchler, Nucl. Phys. **84**, 177 (1966).
[30] A. Bohr and B. R. Mottelson, *Nuclear Structure* (Benjamin, Reading, MA, 1975), Vol. II.
[31] S. S. Hanna, in *Giant Multipole Resonances*, edited by F. E. Bertrand (Harwood, New York, 1980), Table I.
[32] D. E. DiGregorio, M. diTada, D. Abriola, M. Elgue, A. Etchegoyen, J. O. Fernández Niello, A. M. J. Ferrero, S. Gil, A. O. Macchiavelli, A. J. Pacheco, J. E. Testoni, P. R. Silveira Gomes, V. R. Vanin, R. Liguori Neto, E. Crema, and R. G. Stokstad, Phys. Rev. C **39**, 516 (1989).
[33] N. G. Nicolis *et al.*, following paper, Phys. Rev. C **48**, 2895 (1993).
[34] J. Wilczyński, K. Siwek-Wilczyńska, J. Van Driel, S. Gonggrijp, D. C. J. M. Hageman, R. V. F. Janssens, J. Lukasiak, R. H. Siemssen, and S. Y. Van der Werf, Nucl. Phys. **A373**, 109 (1982).
[35] S. Landowne and C. H. Dasso, Phys. Lett. **138B**, 32 (1984).
[36] C. H. Dasso and S. Landowne, Comput. Phys. Commun. **46**, 187 (1987).
[37] S. Raman, C. H. Malarkey, W. T. Milner, C. W. Nestor, Jr., and P. H. Stelson, At. Data Nucl. Data Tables **36**, 1 (1987).
[38] R. H. Spear, At. Data Nucl. Data Tables **42**, 55 (1989).
[39] R. A. Broglia, C. H. Dasso, S. Landowne, and G. Pollarolo, Phys. Lett. **133B**, 34 (1983).